ELSEVIER

Thin Solid Films 393 (2001) 161–167

thin solid films

www.elsevier.com/locate/tsf

Quantum transport in low-dimensional organic nanostructures

J.G. Park[a], G.T. Kim[b], J.H. Park[a], H.Y. Yu[a], G. McIntosh[a], V. Krstic[b], S.H. Jhang[a], B. Kim[a], S.H. Lee[a], S.W. Lee[a], M. Burghard[b], S. Roth[b], Y.W. Park[a,*]

[a] *School of Physics and Condensed Matter Research Institute, Seoul National University, Seoul 151-747, South Korea*
[b] *Max Planck Institut für Festkörperforschung, Heisenbergstrasse 1, D-70569 Stuttgart, Germany*

Abstract

We have studied three low-dimensional systems with sub-micron dimensions: a single polyacetylene (PA) nanofiber; a single-walled carbon nanotube (SWNT)-rope; and a lithographically prepared stripe of poly(2-methoxy-5-(2-ethyl hexyloxy)-*p*-phenylene vinylene) (MEH-PPV). In each case, the sample was contacted to four-probe electrodes, with 100-nm spacing and various electronic transport properties such as the I–V characteristics, the temperature dependence of resistivity and the gate voltage dependence of the transport current were measured. The PA nanofiber was found to be non-ohmic with a room temperature conductivity of ~ 0.1 S/cm. Its carriers were found to be hole-like with charge carrier mobility of $\mu = 7.76 \times 10^{-2}$ cm^2/Vs. For the SWNT-rope, the temperature-dependence of resistivity exhibited signatures of a Luttinger liquid for temperatures below 30 K. With varying gate voltage, periodic peaks were seen in the nanotube current which would normally be attributed to the effects of Coulomb blockade. Interestingly, these peaks show three-way splitting, similar to observations in triple quantum dot experiments. The MEH-PPV stripe, which was produced using electron beam lithography, had I–V characteristics similar to that of a large band-gap semiconductor. In the high field region, these characteristics could be explained in terms of a single carrier device model which considers the field-dependent mobility along with space charge limited conduction (SCLC). All three samples can be considered as field-effect transistors (FETs), with potential use in future high density integrated electronic devices.

Keywords: Elelctrical transport; Polyacetylene; Nanotube; MEH-PPV; FET

1. Introduction

Remarkable developments in nano-science and technology have been made in the last two decades. Nanofabrication techniques in semiconductor research have accelerated the interest in nanostructured materials. These nanostructures include many kinds of organic materials, from molecule to oligomer to polymer, and even biological materials are investigated in detail for demonstration of molecular electronics [1]. Since Aviram and Ratner have suggested molecular rectifiers [2], many possible structures have been suggested and demonstrated. Nowadays, even single molecule like C_{60} or benzene-1,4-dithiol are measured using nanogap electrodes made from electromigration or mechanically controlled breakjunctions (MCB) [3,4]. One of the most feasible molecular electronic devices in organic materials is the carbon nanotube field-effect transistor (FET) [5] and the C_{60} amplifier [6]. In addition, many organic transistors [7,8] and other electronic devices are realised without going to the molecular level but remaining at the micro-scale. These results involve conventional top-down lithographic processes while, in contrast, bottom-up processes are involved in molecular electronic devices.

Conjugated polymer/oligomers are good candidates for this purpose because their π orbital electrons are

* Corresponding author. Tel.: +82-2-880-6607; fax: +82-2-873-7037.
E-mail address: ywpark@phya.snu.ac.kr

0040-6090/01/$ - see front matter
PII: S0040-6090(01)01064-1

easily decollated for contribution to conduction. Polyacetylene (PA) has simple chemical structure and is highly conducting when it is doped. In addition, it has a fibrous structure with a diameter of several tens of nanometer, which can be used as a molecular wire. Another well-known material used in red organic light emitting diodes (OLEDs) is MEH-PPV. Lithographic patterning of organic polymers facilitates their application to electronic devices. There have been several attempts to measure transport properties of conjugated polymer at the sub-micron scale [9]. The gate dependence measurements were carried out on thin films of Durham route polyacetylene [10]. However, no gate dependence was observed on PA single fibber. Carbon nanotubes have been considered a most promising nanomaterial due to their small diameter of 1–2 nm for single-walled nanotubes and 10–50 nm for multi-walled nanotubes. In the case of the metallic nanotubes, single electron transistor action has been observed at low temperatures [11] and the semiconducting nanotubes can be used as field-effect transistors, even at room temperature [5].

In this paper, we present the results of electronic transport measurements of a PA nanofiber, an individual SWNT-rope and a stripe of MEH-PPV. This provides three different examples of low-dimensional synthetic wires and it is of interest to compare and contrast the behaviour of each.

2. Sample preparation and measurement

Networks of PA nanofibers were prepared with dilute Ziegler-Natta catalyst with toluene as the solvent [12]. After exposure to acetylene, the catalyst was thoroughly washed with toluene to obtain purified, low density PA. Using centrifugation, the toluene was first replaced by 2-propanol, which was in turn replaced by a 1:1 mixture of 1 wt.% aqueous solution of sodium dodecyl sulfate (SDS, Aldrich) and Triton X-100 (Aldrich), respectively. After disintegrating the PA network by ultrasonic treatment, one droplet of dispersion was placed on a substrate equipped with four Pt electrode lines separated by ~ 100 nm. Prior to nanofiber deposition, the substrate surface was modified with 0.1 vol.% *N*-[3-(trimethoxysilyl)propyl]-ethylenediamine (Aldrich) to facilitate adsorption. The heavily n-doped (As^+) silicon wafer with a thermally grown oxide layer of 300-nm thickness served as a back gate. As shown in the scanning force microscope (SFM) image of Fig. 1A, there are two kinds of PA nanofibers on top of the Pt electrode. One is a thick nanofiber while the other is a thin one. Generally, the diameter of a PA nanofiber is approximately 20 nm with thinner branches of less than 10 nm. The PA nanofibers are doped with vapour phase iodine for 7 h with in situ monitoring of resistance at $V_{DS} = 40$ mV.

The preparation procedure for the carbon nanotube is similar to the PA nanofiber except for the electrode material and surfactant. Single-walled carbon nanotubes (SWNTs) are produced using the arc-discharge method with Ni/Y as the catalyst and purified using the size exclusion chromatography (SEC) [13]. An amount of 1 mg raw carbon nanotube was dispersed in 0.3 wt.% SDS solution using ultrasonic treatment for 5 min and passed through chromatography column densely packed with controlled pore glass (CPG 3000A, Fluka). One droplet of first or second fraction was placed on the electrodes. In the case of the carbon nanotube we used Au or AuPd electrodes. Fig. 1B shows a SWNT-rope on top of these electrodes. The SWNT-rope is clearly seen near the upper edge of the electrodes. We also observe a bulge in the SWNT bundle between the middle two electrodes, possibly due to a catalyst impurity.

MEH-PPV desolved in *p*-xylene was spun onto electrodes patterned substrate and then exposed to an electron beam from the scanning electron microscope (SEM). The e-beam exposed area is unsolved in solvent

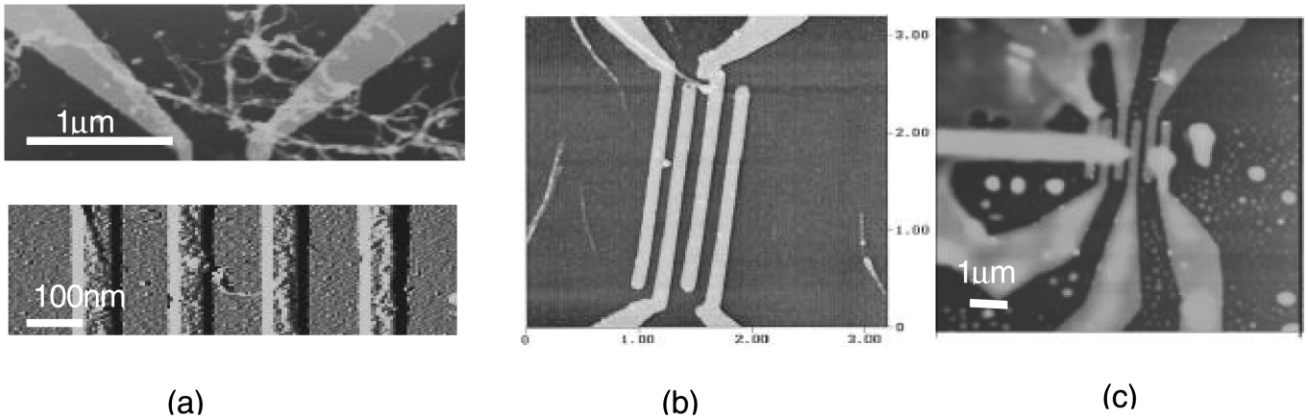

Fig. 1. SFM image of low dimensional nanostructures (A) thick and thin PA nanofiber with diameter of 20 nm and 4.4 nm, respectively, (B) SWNT-rope on top of AuPd electrodes and (C) e-beam patterened MEH-PPV line on top of Pt electrodes.

to form the intended pattern. For the MEH-PPV deposition we used Pt electrodes with 200-nm separation for hole injection. Fig. 1C shows the e-beam patterned line for MEH-PPV. The FT-IR spectroscopy results of the patterned MEH-PPV showed that the peak positions were the same as those of the unirradiated MEH-PPV [14]. This indicated that the original MEH-PPV structure was maintained in the irradiated polymer.

3. PA nanofiber

The I–V characteristics for the thick PA nanofiber ($d \sim 20$ nm) are shown in Fig. 2. At room temperature they are quasi-linear with conductivity $\sigma \sim 0.1$ S/cm. They show non-linear characteristics and this becomes more significant as temperature decreases. The I–V characteristics are different from that of conventional semiconductor transistors [15] or organic field-effect transistors (FETs) [7,8], which show saturation behaviour. This non-saturation behaviour could be originated from the high contact resistance. The lower inset of Fig. 2 shows the transfer characteristics for the thick nanofiber. We note that the current is enhanced at negative gate voltage and suppressed at positive gate voltage. Similar gate voltage dependent I–V characteristics were observed in carbon nanotube FETs [5]. This confirms that the charge carriers are holes in the iodine doped PA nanofiber.

If we consider the low voltage ohmic region in the I–V characteristics in terms of the linear region in conventional MOSFETs, then from the transconductance [15]

$$g_m \equiv \left.\frac{\partial I_{DS}}{\partial V_g}\right|_{V_{DS}=\text{const}} = -\frac{Z}{L}\mu_p C_i V_{DS} \quad (1)$$

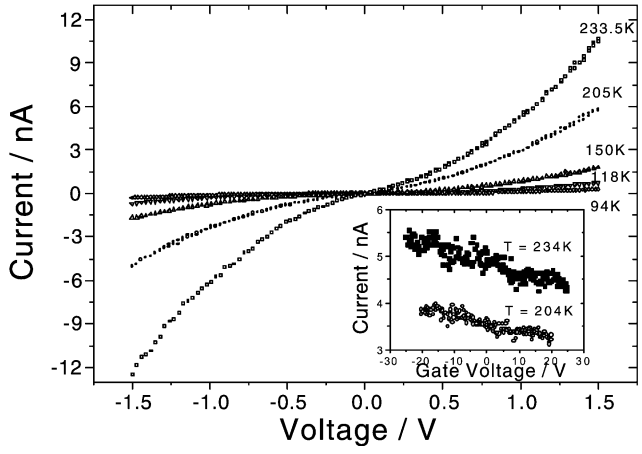

Fig. 2. I–V characteristics of thick PA nanofiber ($d \sim 20$ nm) as a function of temperature. Inset shows transfer characteristics of this nanofiber at $V_{DS} = 1.0$ V.

we can estimate the field-effect mobility, where Z is the channel width, L is the channel length and C_i is the capacitance per unit area. At $T = 233$ K, the transconductance $g_m \approx 2 \times 10^{-11}$ S. Hence, $L = 900$ nm, $Z = 20$ nm and $C_i = 1.2 \times 10^{-8}$ F/cm^2 [16] gave the mobility $\mu = 7.76 \times 10^{-2}$ cm^2/Vs. At $T = 204$ K, the mobility is $\mu = 6.1 \times 10^{-2}$ cm^2/Vs, thus the activation energy of the mobility is estimated to be 33 meV. Here, we assume the nanofiber diameter as the channel width. This is an overestimation of the mobility since many side branches are connected to the thick fibers, thus Z should be larger than 20 nm.

More pronounced gate-dependent I–V characteristics are shown in Fig. 3. Fig. 3A shows the I–V characteristics and Fig. 3B shows the differential conductance ($\partial I_{DS}/\partial V_{DS}$) plot of the thin PA nanofiber ($d \sim 4.4$ nm) as a function of gate voltage. The gate dependence is saturated approximately at $V_g = -5$ V. In contrast to this, the gate-dependent I–V characteristics and differential conductance of the aged thick PA nanofiber ($d \sim 20$ nm), shown in Fig. 3C,D, have non-saturated behaviour. The gate voltage-induced leakage current is checked to be less than 10 pA up to $V_g = 25$ V for the thin nanofiber, 3 pA up to $V_g = 60$ V for the thick nanofiber. A delay time maximum of up to 60 s per gate step is maintained between each I–V characterisation to relax the equilibrium potential distribution. Ageing was done in ambient atmosphere for 2 days.

The case of the thin PA nanofiber shows a different gate voltage dependence which can be separated into two regions across $V_g = -5$ V as the boundary (Fig. 3A,B). This can be clearly seen in gate dependence of the channel conductance ($V_{DS} < 0.24$ V) in Fig. 4. The slope of the channel conductance:

$$g_D \equiv \left.\frac{\partial I_{DS}}{\partial V_g}\right|_{V_g=\text{const}} = -\frac{Z}{L}\mu_p C_i (V_g - V_T) \quad (2)$$

also gives a mobility [17] for the thin PA nanofiber. At the enhanced region (that is, negative gate voltage region $V_g < -5$ V) the mobility is $\mu = 1.5 \times 10^{-3}$ cm^2/Vs at $T = 233$ K and $\mu = 6.0 \times 10^{-4}$ cm^2/Vs at $T = 204$ K, respectively. Here we used $L = 100$ nm and $Z = 4.4$ nm. From this, the activation energy for the mobility is 130 meV. Threshold voltages (V_T) deduced from the intercept for the gate voltage are 3.7 and 7.4 V, respectively. The mobility of thick PA nanofiber decreases to $\mu = 6.45 \times 10^{-4}$ cm^2/Vs at $T = 233$ K after ageing. Comparing the conductivity and mobility of the PA nanofiber to that of a bulk film, the PA nanofiber is below the semiconductor-metal transition regime with doping concentration less than 1% [18]. The activation energy of mobility is also in this regime.

Clearly, mobilities for the thin nanofiber are lower

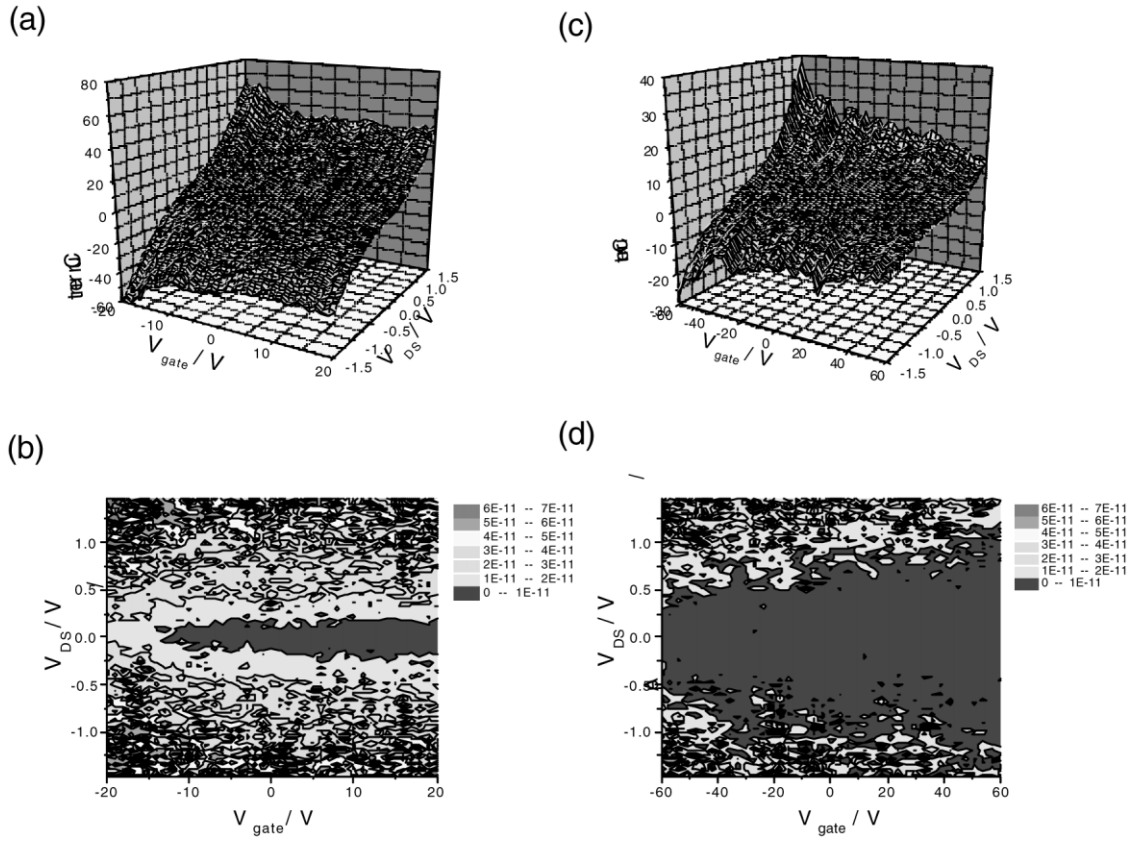

Fig. 3. The gate-dependent I–V characteristics (A,C) and differential conductance ($\partial I_{DS}/\partial V_{DS}$) (B,D) of PA nanofiber. (A) and (B) are the results of thin nanofiber and (C) and (D) are that of aged thick nanofiber. All the measurements were done at 233 K to avoid thermal ageing effect.

than that of the thick nanofiber with associated conductivity being lower than that of the thick nanofiber [19]. Room temperature conductivity for the thin nanofiber is 30 times lower than that of thick nanofiber.

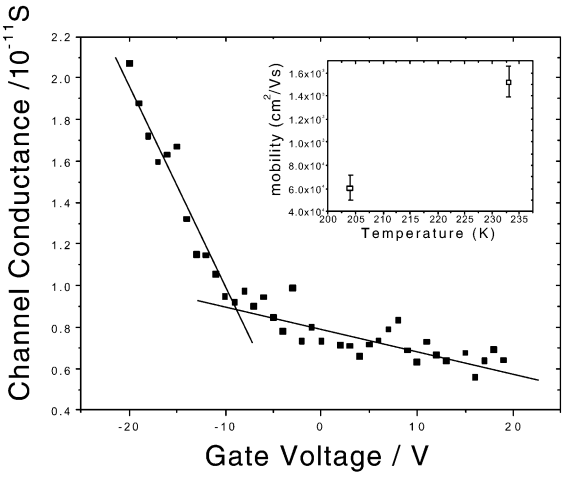

Fig. 4. Channnel conductance of thin PA nanofiber as a function of gate voltage. Apparently, the slope was changed at negative gate voltage due to current enhancement. Solid line is for guidance. Inset shows mobilities at different temperatures. Squares are the mobility of Thin PA nanofiber and the circle is that of aged thick nanofiber.

The lower conductivity of the thin nanofiber is due to its higher surface to volume ratio, thus it is more sensitive to exposed atmosphere during sample preparation. The lower mobility of the aged thick nanofiber can also be explained in terms of its low conductivity. The low activation energy of the mobility for the thick nanofiber is also consistent with its higher conductivity.

4. Single-walled carbon nanotube (SWNT)-rope

In this section we present results of electronic transport measurements for our SWNT-rope sample. To begin with, we examine electrode characteristics. The current vs. voltage I–V characteristics between pairs of electrodes are given in Fig. 5 where the electrodes are labelled as 1-5-4-6 from left to right in Fig. 1B. In Fig. 5, we find that the electrode pairs 1-5 and 5-4 are ohmic with resistances of 4.32 and 2.15 MΩ, respectively. The I–V characteristics of electrodes 4-6 are non-ohmic at this low temperature which would indicate that a barrier potential exists somewhere along this conduction path, possibly due to high contact resistance at electrode 6. Furthermore, for a fixed applied voltage, the current reduces in going from electrode

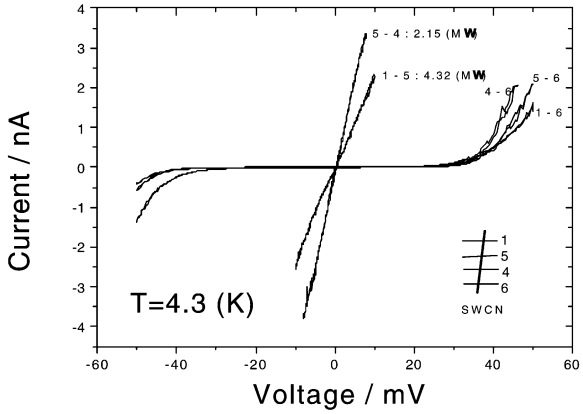

Fig. 5. I–V characteristics of SWNT-rope on top of AuPd electrodes shown in Fig. 1b.

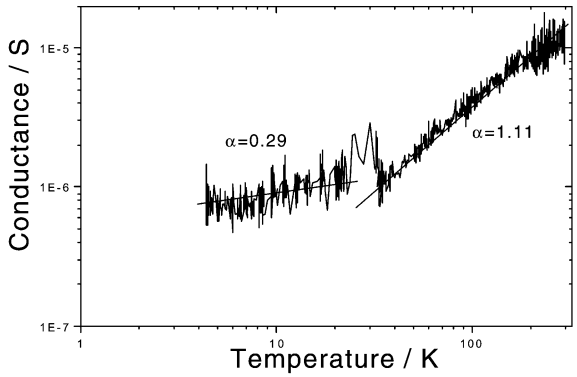

Fig. 6. Log-log plot of temperature dependence of conductance. The fitted lines are due to the conductivity formula $G \sim T^{\alpha}$. Low bias voltage, $V_{DS} = 2$ mV, was applied.

pairs 4-6 to 5-6 to 1-6. This indicates the presence of bulk resistance in the nanotube sample.

Using the four-probe configuration shown in Fig. 1B we have measured the temperature dependence of resistivity for our sample over a temperature range of $T = 4$–300 K. The resulting temperature dependence is shown in Fig. 6 on a log-log scale. It is commonly accepted that metallic carbon nanotubes are one-dimensional metals and, as such, can form a Luttinger liquid. For a Luttinger liquid, the temperature dependence of conductivity is expected to have a power law behaviour, $G \sim T^{\alpha}$ where $\alpha = 0.24$ when the sample lies above the electrodes [20], as for our sample. To pursue this possibility, we fit straight lines to the data yielding a value of $\alpha = 0.29$ for $T < 30$ K. This value is reasonably close to the theoretical value, $\alpha = 0.24$, such that we may be witnessing Luttinger liquid behaviour in our sample for $T < 30$ K. Other workers have witnessed this behaviour over a full temperature range of $T < 300$ K [20]. However, our samples are not individual SWNT but bundles comprising many SWNTs. At higher temperatures thermal activation could increase the inter-tube coupling. Hence, the one-dimensionality and associated Luttinger liquid behaviour would be lost.

Next, we have carried out a two-probe measurement on the electrode pair 4-6. These two electrodes are favoured since the carbon nanotube rope in this region is particularly narrow and well defined. Since the contact resistance of our sample is quite high, the nanotube rope between electrodes 4 and 6 represents a metallic island, separated from the electrodes by tunnelling barriers. If we include a third gating electrode close to the nanotube rope then we will effectively have a single electron tunnelling (SET) transistor. It is well known that the current flow through such a SET transistor displays periodic peaks with varying gate voltage, due to Coulomb blockade [21]. This has been observed for quantum dots [22,23] and for carbon nanotubes [24].

For weak bias voltages, the condition for charge to flow through the SET transistor is given by [21]:

$$Q_0 = C_g V_g = e(n + 1/2) \tag{3}$$

where n is an integer, Q_0 is the charge on the metallic island, C_g is the gate capacitance and V_g is the gate voltage. This yields current peaks which are periodic with varying V_g. Fig. 7 shows the effects of varying the gating voltage on the current flow through electrodes 4-6. We do indeed observe peaks in the current flow with varying gate voltage. However, these peaks display some features, which are not expected for Coulomb blockade. The peaks are not equally spaced but instead increase their spacing with increasing gate voltage.

Interestingly, the peaks in Fig. 7 show three-way splitting. This could be due to the nanotube rope between electrodes 4 and 6 being broken up along its length into three separate metallic regions, separated by insulating barriers. Measurements performed on the analogous situation of three quantum dots in series readily reveal Coulomb blockade peaks with three-way splitting [23]. If the three metallic regions are of ap-

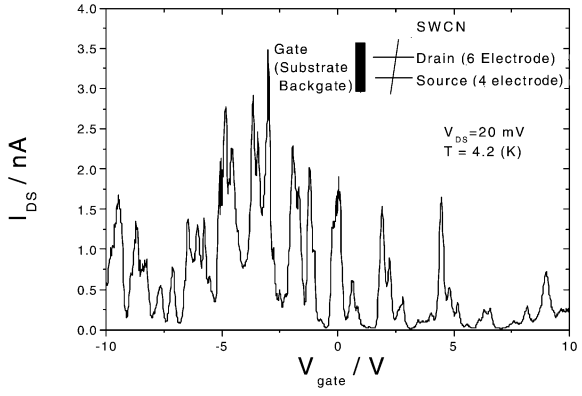

Fig. 7. Gate dependence of Tunneling current at a fixed bias voltage $V_{DS} = 20$ mV.

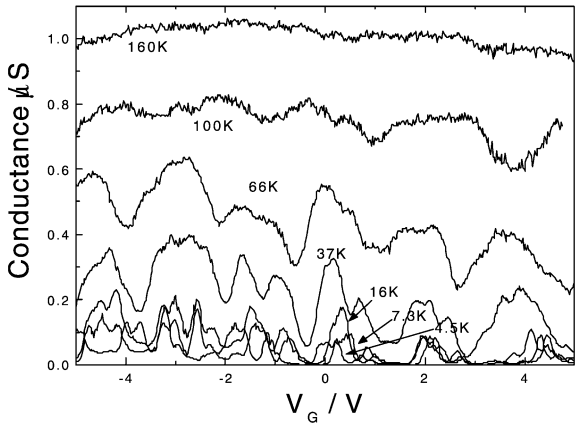

Fig. 8. Variation of Tunneling current as increasing temperature. The broadening of current peak clearly shows smearing out of Coulomb blockade effect.

proximately equal size, then quantum mechanical interactions between the regions will split up their equal energy levels so as to remove degeneracy in the system. As to why the nanotube rope might split up into separate metallic regions, the nanotubes are a one-dimensional system. Hence, the slightest presence of disorder is expected to disrupt the metallic state along its length. Even coupling to the substrate could provide a source of disorder [25]. Also, any defects within the nanotubes will introduce a barrier to metallic conduction, since, in one dimension, the defects cannot be circumvented.

The other possible explanation for the peaks in Fig. 7 is the resonant tunnelling. Since the nanotube rope between electrodes 4 and 6 is a confined system, bound states will occur with discrete energy levels. If our SET transistor can be approximated using a square well potential then the energy levels will not be evenly spaced. This could be the case in Fig. 7. Intertubular interation of the nanotube rope could split the energy level, so that the three-way splitting could be generated.

In Fig. 8 we examine the effects of increasing temperature on the current peaks of Fig. 7. As expected, the peaks become thermally spread out with increasing temperature until, at $T = 160$ K, individual peaks can no longer be discerned.

5. MEH-PPV thin stripe

The width and thickness of the e-beam patterned MEH-PPV determined by SFM is 500 and 20 nm, respectively. The separation between two Pt electrodes is 200 nm, which is considered as the channel length. The I–V characteristics show non-ohmic behaviour. This non-ohmic behaviour becomes more pronounced with decreasing temperature. Since the work function of the Pt electrode (5.6 eV) is higher than the HOMO of MEH-PPV (5.4 eV) [26], the Schottky barrier is not likely to be formed at the contact. Thus, this is a hole only device. We measured the central electrode pair (Fig. 1C) only.

Davids et al. [27] presented a unified model including charge injection, charge transport and space charge effect in the organic material. In our device, it is not injection limited but space charge limited due to there being no Schottky barrier for hole injection.

We consider SCLC with electric field and temperature-dependent mobility as suggested by Blom et al. [28,14]:

$$\mu_p(E) = \mu_p(0)\exp(\gamma\sqrt{E}) \tag{4}$$

where $\mu_p(0)$ denotes the mobility at zero field and γ is comparable to the Poole–Frenkel effect. Also:

$$\mu_p(0) = \mu_0\exp\left(-\frac{\Delta}{k_B T}\right). \tag{5}$$

From the fitting results (Fig. 9), the activation energy is $\Delta = 0.038$ eV, and zero field mobility at room temperature is order of 10^{-3} cm^2/Vs. The magnitude of the activation energy is 1 order lower and the zero field mobility is 3 orders larger than that of sandwiched type MEH-PPV devices [29]. This low activation energy and high zero field mobility could be due to the higher cross-linking introduced during the e-beam irradiation.

6. Concluding remarks

We have measured the electrical properties of organic nanostructure in sub-micron scale. Iodine doped PA nanofiber shows non-ohmic I–V characteristics and current enhancement at the negative gate voltage. Hence, doped PA nanofiber can be used as a nanoscale FET as was done in SWNT FET even though the

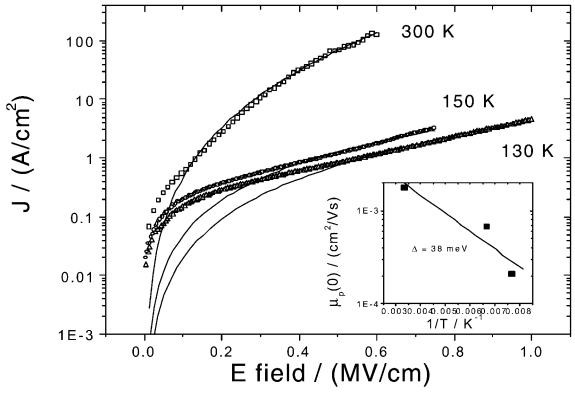

Fig. 9. J–V characteristics of e-beam patterened MEH-PPV. Fitting was done using SCLC with electric field-dependent mobility. Inset shows temperature dependencies of the zero field mobility. Detail fitting parameters are in ref. [14].

on–off ratio and mobility are low. The SWNT-rope is metallic and acts as SET transistor, while a semiconducting SWNT acts as FET. Since the SWNT is one-dimensional, our measurement also reveals Luttinger liquid-like behaviour. MEH-PPV, a semiconducting conjugated polymer, was patterned using e-beam and showed non-ohmic I–V characteristics with improved mobility. This could be originated from the increased cross-linking and ordering.

Realization of nanoscale transistors using organics — a PA nanofiber or a SWNT — make it possible for use in future information technology. Also MEH-PPV patterning can be used as nano electroluminescence (EL) devices. Even though integration of these molecular electronic devices is the most crucial barrier, its realisation could yield the tera-bit memory devices for future electronics.

Acknowledgements

This work was supported by KISTEP under the contract No. 98-I-01-04-A-026, Ministry of Science and Technology (MOST), Korea. M. B. is grateful to the Deutsche Forschungsgemeinschaft (DFG) for financial support.

References

[1] M.C. Petty, M.R. Bryce, D. Bloor (Eds.), Introduction to Molecular Electronics, Edward Arnold, London, 1995.
[2] A. Aviram, M.A. Ratner, Chem. Phys. Lett. 29 (1974) 277.
[3] H. Park, J. Park, A.K.L. Lim, E.H. Anderson, A.P. Alivisatos, P.L. McEuen, Nature 407 (2000) 57.
[4] M.A. Reed, C. Zhou, C.J. Muller, T.P. Burgin, J.M. Tour, Science 278 (1997) 252.
[5] S.J. Tans, A.R.M. Verschueren, C. Dekker, Nature 393 (1998) 49.
[6] C. Joachim, J.K. Gimzewski, Chem. Phys. Lett. 265 (1997) 353.
[7] G. Horowitz, R. Hajlaoui, D. Fichou, A.E. Kassmi, J. Appl. Phys. 85 (1999) 3202.
[8] L. Torsi, A. Dodabalapur, L.J. Rothberg, A.W.P. Fung, H.E. Katz, Phys. Rev. B 57 (1998) 2271.
[9] S.H.M. Persson, P. Dyreklev, O. Inganas, Adv. Mater. 8 (1996) 405.
[10] J.H. Burroughes, C.A. Jones, R.H. Friend, Nature 335 (1988) 137.
[11] S.J. Tans, M.H. Devoret, H. Dai, A. Thess, R.E. Smalley, L.J. Geerligs, C. Dekker, Nature 386 (1997) 474.
[12] G.E. Wnek, J.C.W. Chien, F.E. Karasz, M.A. Dury, Y.W. Park, A.G. MacDiarmid, A.J. Heeger, J. Polym. Sci.: Ploym. Lett. Ed. 17 (1979) 779.
[13] G.S. Duesberg, J. Muster, V. Krstic, M. Burghard, S. Roth, Appl. Phys. A 67 (1998) 117.
[14] J.H. Park, H.Y. Yu, J.G. Park, B. Kim, S.H. Lee, Y.W. Park, Thin Solid Film, (2001) this issue.
[15] S.M. Sze, Semiconductor Devices Physics and Technology, Wiley, New York, 1985.
[16] R.C. Haddon, A.S. Perel, R.C. Morris, T.T.M. Palstra, A.F. Hebard, R.M. Fleming, Appl. Phys. Lett. 67 (1995) 121.
[17] W.A. Schoonveld, J. Vrijmoeth, T.M. Klapwijk, Appl. Phys. Lett. 73 (1998) 3884.
[18] Y.W. Park, A.J. Heeger, M.A. Dury, A.G. MacDiarmid, J. Chem. Phys. 73 (1980) 946.
[19] A.R. Brown, D.M. de Leeuw, E.E. Havinga, A. Pomp, Synth. Met. 68 (1994) 65.
[20] M. Bockrath, D.H. Cobden, J. Lu, A.G. Rinzler, R.E. Smalley, L. Balents, P.L. McEuen, Nature 397 (1999) 598.
[21] H. Grabert, M.H. Devoret, Single Charge Tunneling, Plenum Press, New York, 1992.
[22] A. Furusaki, K.A. Matveev, Phys. Rev. Lett. 75 (1995) 709.
[23] F.R. Waugh, M.J. Berry, D.J. Mar, R.M. Westervelt, K.L. Campman, A.C. Gossard, Phys. Rev. Lett. 75 (1995) 705.
[24] S.J. Tans, M.H. Devoret, R.J.A. Groeneveld, C. Dekker, Nature 394 (1998) 761.
[25] C.T. White, T.N. Todorov, Nature 393 (1998) 240.
[26] I.H. Campbell, T.W. Hagler, D.L. Smith, J.P. Ferraris, Phys. Rev. Lett. 76 (1996) 1900.
[27] P.S. Davids, I.H. Campbell, D.L. Smith, J. Appl. Phys. 82 (1997) 6319.
[28] P.W.M. Blom, M.J.M. de Jong, M.G. van Munster, Phys. Rev. B 55 (1997) R656.
[29] J.M. Lupton, I.D.W. Samuel, J. Phys. D: Appl. Phys 32 (1999) 2973.